Bulletin of Geophysics and Oceanography Vol. 67, n. 2, pp. 295-324; June 2026
DOI 10.4430/bgo00534

Evaluation of proxies of the averaged shear-wave velocity to a depth of 30 m (*Vs*30) for site characterisation in Italy

G. Brunelli[1], S. Sgobba[1], E.M. Thompson[2], D.J. Wald[2], G. Lanzano[1] and L. Luzi[1]

[1] *Istituto Nazionale di Geofisica e Vulcanologia, Sezione di Milano, Milano, Italy*
[2] *U.S. Geological Survey, Golden, CO, U.S.A.*

(Received: 9 October 2025; accepted: 3 April 2026; published online: 10 June 2026)

ABSTRACT Near-surface geological conditions strongly influence seismic ground motion, and the time-averaged shear-wave velocity to a depth of 30 m (*Vs*30) is a commonly used parameter to describe site effects in ground-motion models applied in shaking scenarios and seismic hazard assessment. However, the limited availability of direct *Vs* measurements has led to the growing use of morphometric and geological proxies. This study examines the relationship between *Vs*30 and a comprehensive set of topographic and lithological proxies across Italy, utilising a dataset comprising approximately 15,000 *Vs* profiles distributed across Italy compiled from seismic microzonation studies, regional databases, and the ITalian ACcelerometric Archive (ITACA). Topographic proxies were derived from the high-resolution (10 m) national digital terrain model, resampled to multiple spatial scales (150–1000 m), while lithological information was obtained from the national maps and complemented by global soil thickness data. This study provides the first nationwide assessment of multi-proxy correlations with *Vs*30 in Italy and establishes the foundation for the development of a robust, spatially continuous, and lithologically informed *Vs*30 model.

Key words: *Vs*30 dataset, topographic proxies, correlation analysis, lithological classification.

1. Introduction

Numerous earthquakes have demonstrated that near-surface geological conditions can significantly impact both the amplitude and the spatial distribution of shaking and damage. Well-known examples include the 1985 M_w 8.1 Michoacán earthquake (Singh and Ordaz, 1993), the 1989 M_w 6.9 Loma Prieta event (Hough *et al*., 1990), and the 1994 M_w 6.7 Northridge earthquake (Spudich *et al*., 1996), all of which highlighted the role of local site amplification. These cases confirm that, alongside source and path effects, site effects are a fundamental factor in shaping ground-motion intensities (Aki, 1988; Boore *et al*., 1997; Field, 2000).

The use of *Vs*30, defined as the time-averaged shear-wave velocity to a depth of 30 m, was formally introduced by Borcherdt and Glassmoyer (1995) to unambiguously describe site classes and coefficients for the 1994 United States National Earthquake Hazards Reduction Program (NEHRP) (Martin and Dobry, 1994), and was subsequently adopted worldwide. Its popularity stems from the fact that it is a simple metric that can be obtained by means of noninvasive surface-wave methods (Yong *et al*., 2016).

Nowadays, *Vs*30 is commonly used to account for site effects in empirical ground-motion models (Abrahamson and Silva, 2008; Boore and Atkinson, 2008; Campbell and Bozorgnia, 2008;

Chiou and Youngs, 2014; Lanzano *et al*., 2019), for the identification of soil categories in seismic codes (CEN, 2004; MIT, 2018) and to derive seismic risk maps.

However, despite its widespread use, several studies have pointed out that *Vs*30 does not fully capture the complexity of local seismic response, especially in the presence of strong velocity impedance contrasts and in deep sedimentary basins (Lee and Trifunac, 2010; Paolucci *et al*., 2021). These limitations have encouraged a gradual shift towards multi-parameter site-characterisation frameworks. In Italy, the updated seismic code NTC 2018 (MIT, 2018) introduces equivalent shear-wave velocity as an alternative to *Vs*30, incorporating the depth to the engineering bedrock, defined by a shear-wave velocity of 800 m/s. Similarly, Pitilakis *et al*. (2018) and other authors note that *Vs*30 is not always the most appropriate descriptor of site amplification under all conditions, and that complementary parameters such as deposit thickness and site fundamental frequency or period should also be considered. Nevertheless, *Vs*30 still remains the most used proxy of seismic site amplification. However, the cost and logistical effort of geophysical tests to measure the shear-wave velocity profile prevent the systematic application across large areas. This limitation has motivated the development of alternative approaches to retrieve *Vs*30 based on proxies, which enable cost-effective and spatially continuous estimates of this parameter.

In this perspective, the present study provides an initial step towards assessing which large-scale, spatially continuous proxies may contribute to more comprehensive and operational site-characterisation approaches in Italy.

Among these, topographic slope has become one of the most widely used proxies due to the global availability of digital elevation models (DEMs). Wald and Allen (2007) first proposed slope alone as a global proxy for *Vs*30, relying on the empirical observation that stiffer materials tend to sustain steeper slopes, whereas softer sediments commonly occur in flatter terrains. While conceptually simple and computationally efficient, slope-only models often introduce regional biases (Yong *et al*., 2012). To overcome these limitations, subsequent studies combined slope with additional geological information. For instance, Thompson *et al*. (2014) and Wills *et al*. (2015) integrated slope with surface geology in California, significantly improving predictive performance and reducing regional biases.

Other works have emphasised the role of the depositional setting, noting that environments such as alluvial fans, lacustrine basins, or colluvial deposits exhibit distinct velocity patterns even when slopes are similar (Yong *et al*., 2012; Parker *et al*., 2017; Choi *et al*., 2025). Additional improvements come from including sediment thickness and basin structure, which control the depth to bedrock and the impedance contrast at shallow depths, thereby influencing surface amplification (Parker *et al*., 2017; Loviknes *et al*., 2024; Geyin and Maurer, 2023). Similarly, the geological age of formations has proven useful, as younger and unconsolidated sediments are generally associated with lower *Vs*30 values, whereas older and more consolidated rocks, such as carbonates or crystalline units, yield higher velocities (Crespo *et al*., 2022; Navarro *et al*., 2025).

In Italy, interest in the detailed study of site effects has substantially grown following recent damaging earthquakes, such as the 2002 San Giuliano di Puglia event [M_w 5.7: Strollo *et al*. (2007); Puglia *et al*. (2013)], the 2009 L'Aquila earthquake [M_w 6.3: Tertulliani *et al*. (2012)], and the 2012 Emilia seismic sequence [M_w 6.1; Luzi *et al*. (2013)], which clearly demonstrated the critical role of local site conditions in amplifying shaking and controlling damage distribution. Following these earthquakes, the Italian Civil Protection Department launched large-scale seismic microzonation (SM) campaigns, producing a unique national dataset of geophysical measurements (Web MS-CLE, n.d). In recent years, Forte *et al*. (2019) developed a seismic soil classification map for Italy by averaging site-specific *Vs*30 measurements for each geo-lithological

complex derived from a 1:100,000 geological map. Mori *et al*. (2020) produced a high-resolution *Vs*30 map by combining geomorphological classes with regression models based on slope and elevation, using the Italian SM dataset of 11,000 *Vs* profiles; more recently, Mori *et al*. (2026) calibrated another *Vs*30 map with the aid of machine learning techniques. In this work, we test the correlation between *Vs*30 and topographic and morphologic proxies that have not been used in previous works on a national scale in Italy.

On a regional scale, Gironelli *et al*. (2024) developed a *Vs*30 map for the Marche region (Italy) using a dual-proxy mixed-effect regression, where *Vs*30 was modelled as a function of reclassified lithological complexes from the 1:100,000 lithological map of Italy (ISPRA, 2021) proposed by the Istituto Superiore per la Protezione e la Ricerca Ambientale [the Italian Institute for Environmental Protection and Reasearch (ISPRA)] and topographic slope. Importantly, the study demonstrated that the original 30-metre resolution could be resampled to 150 m without significant loss of variability in terms of *Vs*30.

On a global scale, beyond the United States Geological Survey global slope-based *Vs*30 map (Wald and Allen, 2007), Japan's Seismic Hazard Information Station derives amplification factors from nationwide engineering-geomorphologic classifications linked to *Vs* profiles (Wakamatsu and Matsuoka, 2011), and New Zealand's national *Vs*30 maps blend geology-based and terrain/slope-based models (Perrin *et al*., 2015; Foster *et al*., 2019).

Collectively, these studies confirm that incorporating geological/lithological information alongside morphometric variables is essential for multi-proxy approaches, leading to more accurate and regionally transferable *Vs*30 estimates.

In addition to these contributions, Stewart *et al*. (2014) performed one of the most comprehensive evaluations of geology- and terrain-based proxies for *Vs*30, using a database of 314 shear-wave velocity profiles from the Hellenic region. Their analysis showed that surface-geology categories, defined according to geologic age, material gradation, and depositional environment, provide substantially more accurate estimates of *Vs*30 than models based solely on terrain slope. More recently, Cultrera and Mercuri (2025) investigated site-effect indicators at stations of the Istituto Nazionale di Geofisica e Vulcanologia [the Italian National Institute of Geophysics and Volcanology (INGV)] seismic network and found that lithological information is significantly correlated with the spatial variability of site response. These findings further reinforce the importance of robust geological and lithological descriptors when analysing the variability of *Vs*30 on a national scale.

Building on these national and international experiences, the present study aims to investigate the correlation between *Vs*30 and a comprehensive set of site proxies on a national scale. Starting from the high-resolution national digital terrain model (DTM) TINITALY/1.1 (Tarquini *et al*., 2023), we tested different spatial scales by resampling the DTM onto coarser grids. From these, we derived several indicators describing terrain shape and variability, such as *slope*, measures of landscape *roughness* and *curvature*, as well as geomorphological classes. To complement the terrain information, we also include independent geological data, specifically sediment thickness (Pellettier *et al*., 2016) and lithological classifications from national sources (ISPRA, 2021; Bucci *et al*., 2022).

The aim of this work is threefold: i) to test, for the Italian territory, the predictive performance of multiple morphometric and geological proxies against an extensive *Vs*30 database, so as to explain *Vs*30 variability; ii) to assess the ability of existing lithological maps to capture *Vs*30 variability; and iii) to propose a new lithological reclassification on a national scale, based on the ISPRA (2021) lithological map, that better reflects the spatial distribution of *Vs*30.

2. Data sources

2.1. Vs*30 dataset*

The velocity profiles in this study are derived from different data sources, such as SM studies, geodata sets of Italian regions, professional studies, and the ITalian ACcelerometric Archive [ITACA: Felicetta *et al*. (2023)] database.

Approximately 15,000 shear-wave velocity (*Vs*) profiles were collected throughout Italy through active and passive surveys, employing both invasive and noninvasive techniques, as well as combined approaches. These profiles were obtained from geophysical measurements conducted using methods such as down-hole, cross-hole, seismic refraction (P- and S-wave methods), multi-channel analysis of surface waves (MASW) in both Love and Rayleigh waves (Park *et al*., 1999; Safani *et al*., 2005), spatial autocorrelation (SPAC) and derivative approaches (Aki, 1957; Asten, 2006; Stephenson *et al*., 2009), and refraction microtremor [ReMi: Louie (2001)].

Fig. 1a illustrates the spatial distribution of the *Vs*30 values, where low values are represented in blue and high values in red. Fig. 1b shows the main geographic and physiographic features and administrative regions referenced in the paper. The final dataset contains a few *Vs*30 profiles with high values (rock sites), which are primarily located along the Apennine arc, south-eastern Sicily, the Alps, and the Puglia region. The lowest *Vs*30 values are predominant in the Po Plain and coastal areas, as expected.

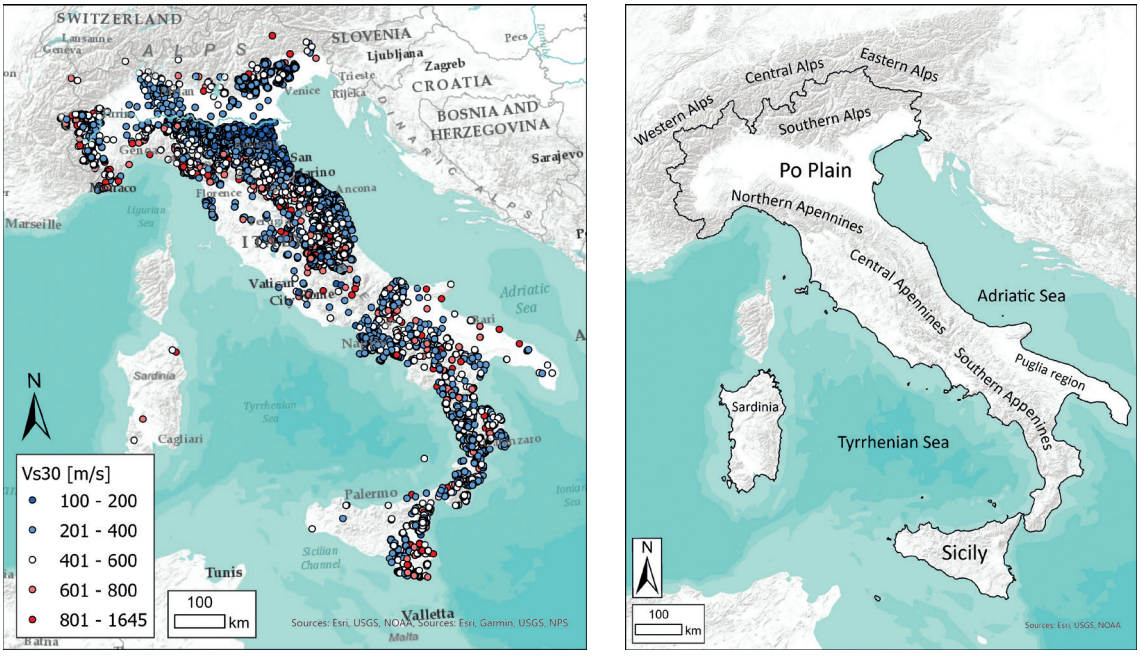

Fig. 1 - a) Spatial distribution of the *Vs*30 dataset. b) Map of the main geographic and physiographic features and administrative regions referenced in the paper.

The histogram of the 10-base logarithm of *Vs*30, shown in Fig. 2, reveals a bimodal distribution, with a first peak around 2.4 (*Vs*30 ≈ 250 m/s) and a second peak near 2.6 (*Vs*30 ≈ 400 m/s). This pattern reflects the presence of profiles acquired in fine-grained deposits, medium to coarse-grained deposits, and rocks affected by fracturing and/or alteration. The distinction among these geological features underscores the importance of accounting for lithological contribution when analysing *Vs*30.

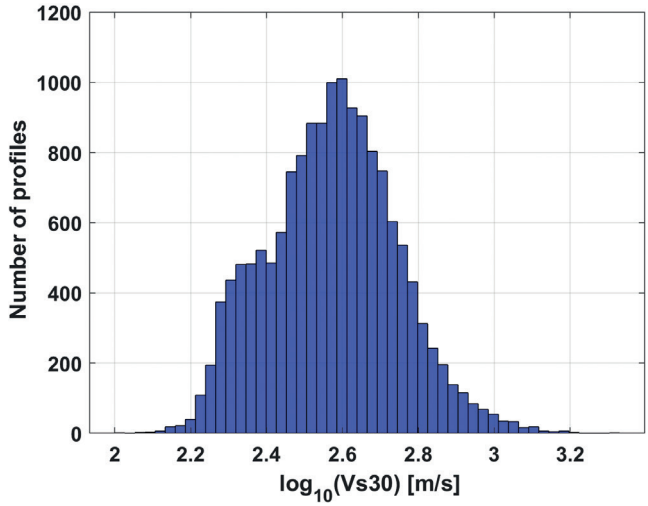

Fig. 2 - Histogram of $\log_{10}$(*Vs*30).

2.2. Lithological maps

Lithology captures essential information about the composition and physical and mechanical characteristics of rocks and soils, making it a crucial factor in understanding the Earth's surface and subsurface processes. Lithological data is typically derived from geological maps and substantial efforts have been made in recent years to improve global accessibility to high-quality geological datasets (EPOS, n.d.).

In Italy, geological maps having nationwide coverage are available at scales of 1:1,250,000 (Bonomo *et al*., 2005), 1:1,000,000 (Compagnoni, 2004; Cipolloni *et al*., 2009; Pantaloni, 2011), 1:500,000 (Compagnoni *et al*., 1976–1983), and 1:100,000 (ISPRA, 2020), all distributed by ISPRA (Delogu *et al*., 2012). Additionally, ISPRA coordinates and publishes the 1:50,000 geological map of Italy, although it currently offers only partial coverage of the national territory. In particular, the digital 1:100,000 lithological map was released in 2021, based on the 277 sheets of the geological map of Italy (ISPRA, 2020); it provides a consistent lithological representation, of the entire country, with no discontinuities at map borders, subdivided into 50 classes identified from geological descriptions and age, whose detailed descriptions are reported in Table A1 of Appendix A. This effort resulted in a single shapefile, which is accessible through web services (ISPRA, 2021).

An alternative lithological map of Italy at a 1:100,000 scale was proposed by Bucci *et al*. (2021, 2022) and derived from the nationwide 1:100,000 geological map of Italy (ISPRA, 2020). The 300,000 polygons are classified into 19 classes according to compositional and geomechanical criteria.

2.3. Average soil and sedimentary deposit thickness map

Pelletier *et al*. (2016) released a high-resolution global dataset (30 arcsec, ~1 km) of soil, intact regolith (heterogeneous material covering solid bedrock), and sedimentary deposit thicknesses above unweathered bedrock, with a maximum thickness of 50 m. The dataset distinguishes between hillslopes, valley bottoms, and lowlands, using optimised models for each landscape type. Thickness estimates are calibrated and validated with independent data: soil thickness measurements from the U.S. and Europe for hillslopes, and depth-to-bedrock observations from groundwater wells in the U.S. for lowlands.

2.4. Digital elevation model and topographic indices

In this study, the TINITALY/1.1 DTM, developed by Tarquini *et al*. (2023) was used. It covers the entire Italian territory, as the primary source of elevation data on the national scale. This model provides a consistent representation of the surface topography, enabling us to derive slope values and related morphometric variables uniformly across the study area. It features a spatial resolution of 10 m × 10 m and is available in GeoTIFF format, georeferenced using the UTM WGS 84 zone 32N coordinate system (INGV Sezione di Pisa, n.d.).

The TINITALY/1.1 DTM, originally available with a spatial resolution of 10 m × 10 m (Tarquini *et al*., 2023), was downsampled to four different spatial resolutions (150 m, 250 m, 500 m, and 1,000 m) using the resample tool in ArcGIS Pro 3.4.2 (Esri Inc., 2024) with the Nearest Neighbour algorithm. No additional filtering or smoothing was applied. This resampling strategy was adopted to evaluate which spatial scale provides the best correlation between terrain-derived proxies and *Vs*30, while preserving the original elevation values and avoiding any interpolation-induced modification of the DEM.

For each resolution, *elevation* was directly extracted from the resampled DEM and the following topographic indices were computed using ArcGIS Pro 3.4.2 (see Table 1 for the definitions of these metrics): i) *slope*, ii) terrain ruggedness index (*TRI*), iii) vector ruggedness measure (*VRM*), iv) topographic position index (*TPI*), v) *profile curvature*, vi) *plan curvature*, vii) *standard curvature*, and viii) geomorphological classes. The *TRI* is calculated using the GDALDEM Roughness function of the Geospatial Data Abstraction Library (GDAL Development Team, 2021), available in QGIS 3.22.11 (QGIS Development Team, 2022).

Slope quantifies the rate of *elevation* change in the direction of the steepest gradient for each DEM cell. As the first derivative of the DEM, it describes the steepness of the terrain at any given point (Fig. 3).

The *TRI* (Fig. A1), introduced by Riley *et al*. (1999), is a measure of terrain roughness that quantifies topographic heterogeneity in a DTM. The *TRI* is widely used in ecological modelling, hydrology, and geomorphology to assess terrain complexity and habitat suitability. Higher *TRI* values indicate rugged or highly variable terrain, while lower values represent flat or smooth surfaces.

The *VRM* (Fig. A2), introduced by Sappington *et al*. (2007), analyses the three-dimensional variability in the orientation of surface normals, which are vectors perpendicular to the terrain. For each grid cell in a DTM, the average direction of the normals from the focal cell and surrounding eight neighbouring cells is calculated. The magnitude of the resultant vector indicates the degree of alignment of the normals for the nine cells. Subtracting this magnitude from 1 produces a dimensionless ruggedness index that ranges from 0 (flat surface) to 1 (highly rugged surface).

Terrain *roughness* (Fig. A3), following Hobson (1972) and Wilson *et al*. (2007), is defined as the maximum *elevation* difference between a focal cell and its surrounding eight neighbouring

Table 1 - Summary of the topographic proxies adopted in this study, including their formal definitions, units, and value ranges. All topographic indices (*slope*, *TRI*, *VRM*, *TPI*, curvatures, and geomorphological classes) were computed from the DEM at a spatial resolution of 150 m × 150 m; therefore, the reported ranges refer to this resolution.

Topographic proxies	Formal definition	Units	Range
Slope	Local terrain slope expressed as the inclination angle with respect to the horizontal plane.	degrees (°)	0–86
TRI (Riley *et al.*, 1999)	$TRI = \sqrt{\sum (x_i - x_0)^2}$ where x_0 is the elevation of the central cell and x_i represents the elevation of each of the eight neighbouring cells.	m	0–6,768
Roughness (Hobson, 1972)	Maximum *elevation* difference between a focal cell and its eight surrounding neighbouring cells.	m	0–3,480
VRM (Sappington *et al.*, 2007)	$VRM = 1 - \frac{\sqrt{(\sum_{i=1}^{N} x_i)^2 + (\sum_{i=1}^{N} y_i)^2 + (\sum_{i=1}^{N} z_i)^2}}{N}$ where x_i, y_i and z_i are the components of the unit vector normal to the surface at the *i*-th cell, computed as: $x_i = sin\ (slope_i) \times sin\ (aspect_i)$ $y_i = sin\ (slope_i) \times cos\ (aspect_i)$ $z_i = cos\ (slope_i)$ where *aspect* is the compass direction that a slope faces and *N* is the number of cells in the moving window (*N* = 9 for a 3×3 window). *VRM* is computed from the sum of the unit normal vectors within the 3×3 cell moving window and assigned to the central cell.	–	0–0.4
TPI (Weiss, 2001)	$TPI = x_0 - \bar{x}$ where x_0 is the *elevation* of the central cell and $\bar{x}$ is the mean is the mean *elevation* of the eight neighbouring cells within the 3×3 window.	m	−1,691–1,265
Standard curvature (Moore *et al.*, 1991; Zevenbergen and Thorne, 1987)	$k = 100 \times \left(\frac{\partial^2 z}{\partial x^2} + \frac{\partial^2 z}{\partial y^2}\right)$ The sum of the second derivatives of *elevation* with respect to the horizontal coordinates.	m^{-1}	-30×10^{-2}–15.3×10^{-2}
Profile curvature (Moore *et al.*, 1991; Zevenbergen and Thorne, 1987)	Curvature calculated along the direction of maximum slope.	m^{-1}	-15.8×10^{-2}–15.2×10^{-2}
Planform curvature (Moore *et al.*, 1991; Zevenbergen and Thorne, 1987)	The curvature of the surface perpendicular to the direction of maximum slope.	m^{-1}	-14.8×10^{-2}–5.4×10^{-2}
Geomorphological classes (Jasiewicz and Stepinski, 2013)	Geomorphological classification derived from a DEM by analysing how *elevation* increases or decreases along the eight main directions around each cell: flat (1), peak (2), ridge (3), shoulder (4), spur (5), slope (6), hollow (7), footslope (8), valley (9), and pit (10).	–	–

cells. High *roughness* values indicate a highly irregular or rugged terrain with significant *elevation* differences, such as mountainous or rocky areas. Low *roughness* values represent smoother, more homogeneous surfaces, such as plains or gently rolling landscapes.

Fig. 3 - *Slope* map expressed in degrees and calculated with a spatial resolution of 150 m; the average value is 9.4°.

The *TPI* (Fig. A4), proposed by Weiss (2001), quantifies the relative *elevation* of a focal cell compared to the average *elevation* of its surrounding neighbourhood. A positive *TPI* indicates that the focal cell is higher than its surrounding cells, characterising ridges, peaks, or elevated landforms. Conversely, a negative *TPI* suggests that the cell is lower than its surrounding cells, identifying depressions, valleys, or concave features. Values near zero imply that the cell has a similar *elevation* to the average of its neighbourhood, corresponding to relatively flat or uniform slopes.

The *profile curvature* (Fig. A5) measures the amount of slope change along a downhill flow path, indicating whether water will speed up or slow down due to the slope's concavity or convexity. A positive *profile curvature* reveals that the surface is upwardly concave (like a valley), which decelerates flow and encourages deposition; a negative value indicates that the surface is upwardly convex (like a hilltop), accelerating flow and promoting erosion.

The *planform curvature* (Fig. A6) (commonly known as *plan curvature*) represents the curvature measured perpendicularly to the direction of the maximum slope. Positive values indicate areas where surface flow diverges, while negative values correspond to zones of converging flow. When *plan curvature* is positive, the surface is convex in the direction perpendicular to the slope, whereas a negative value signifies concavity in the same orientation. A curvature value of zero indicates a flat surface in the analysed direction.

The *standard curvature* (Fig. A7) combines both profile and *planform curvature* into a single metric that summarises overall surface curvature. Analysing the two orthogonal components

(*profile* and *planform curvature*) together help interpret water movement across the terrain and, consequently, soil deposition dynamics.

The geomorphological classes (Fig. A8 and Table 1) are identified following the approach proposed by Jasiewicz and Stepinski (2013). They provide a representation of the landscape based on variations in *elevation* within the local neighbourhood of a target cell. In total, we obtained 498 distinct geomorphon patterns.

Table 2 summarises the *Vs*30 proxies analysed in this study, grouped into categorical and numeric variables.

Table 2 - *Vs*30 proxies analysed in this study, grouped into categorical and numeric variables.

Categorical proxies	Numeric proxies
Lithological maps (ISPRA, 2021; Bucci *et al.*, 2021, 2022); geomorphological classes (Jasiewicz and Stepinski, 2013).	*Elevation; slope; roughness; TRI; VRM; TPI; profile curvature; planform curvature; standard curvature;* average soil and sediment thickness (Pelletier *et al.*, 2016).

3. Statistical analyses

Statistical analyses were performed separately for numerical and categorical variables. In particular, the following statistical indices were used to quantify the relationships between *Vs*30 and the identified proxies (topographic indexes and lithology):

- Pearson correlation coefficient (*r*) (Pearson, 1895) measures the linear correlation between two numerical variables. It ranges from -1 to 1, where 1 indicates a perfect positive correlation, -1 indicates a perfect negative correlation, and 0 indicates no linear correlation;
- eta-square (η^2) index (Fisher, 1925) quantifies the relationship between numerical and categorical variables from the proportion of variance in a numerical variable explained by a categorical variable. It ranges from 0 to 1, where 0 means that the categorical variable does not explain any variation in the numerical variable and 1 means that the categorical variable fully explains the variance in the numerical variable.

3.1. Numerical variables

The slope angle in degrees was converted to its tangent, following Wald and Allen (2007); hereinafter, the term slope refers to this quantity. Pearson correlation coefficients were computed between $\log_{10}$(*Vs*30) and all numerical proxies, repeating the analysis at four spatial resolutions. *TPI*, *standard curvature*, *planform curvature*, and *profile curvature* exhibit only weak linear correlation with $\log_{10}$(*Vs*30), with $|r| \leq 0.15$ at all four spatial resolutions, and were therefore not considered as candidate predictors.

We, then, examined in more detail the relationship between $\log_{10}$(*Vs*30) and the deposit thickness. Among the products provided by Pelletier *et al*. (2016), we specifically used the raster Average_soil_and_sedimentary-deposit_thickness.tif. This global-scale dataset, originally provided at a spatial resolution of approximately 1 km, represents the weighted-average thickness of soil and sedimentary deposits within each grid cell and describes the thickness of relatively porous and unconsolidated materials overlying unweathered geological bedrock, up

to a maximum depth of 50 m (Fig. A9). This depth range is sufficient to investigate potential relationships with *Vs*30. However, it should be noted that this map was developed to support hydrological and ecosystem models; therefore, its objectives differ from those of seismic site characterisation. In addition, in the Italian territory, sediment thickness is known to significantly vary at spatial scales much smaller than 1 km².

A negative Pearson correlation, consistent with expectations, is observed between $\log_{10}$(*Vs*30) and sediment thickness (r = −0.58). However, Fig. 4 shows that the values are mainly clustered into two deposit thickness classes (0–15 m and ≥50 m), with very few intermediate values. A detailed analysis of the raster value distribution over Italy shows that the thickness variable is strongly concentrated in a few recurring discrete values. About 43% of the Italian pixels are assigned a thickness of 1 m and about 15% a thickness of 50 m, so that nearly 60% of the national coverage falls into only two thickness values.

A sensitivity analysis indicates that the observed correlation is controlled by these two dominant end-member classes. When the two most populated thickness values (1 m and 50 m) are excluded, the Pearson correlation decreases from −0.58 to about −0.19. This shows that the global correlation is influenced by these two clusters.

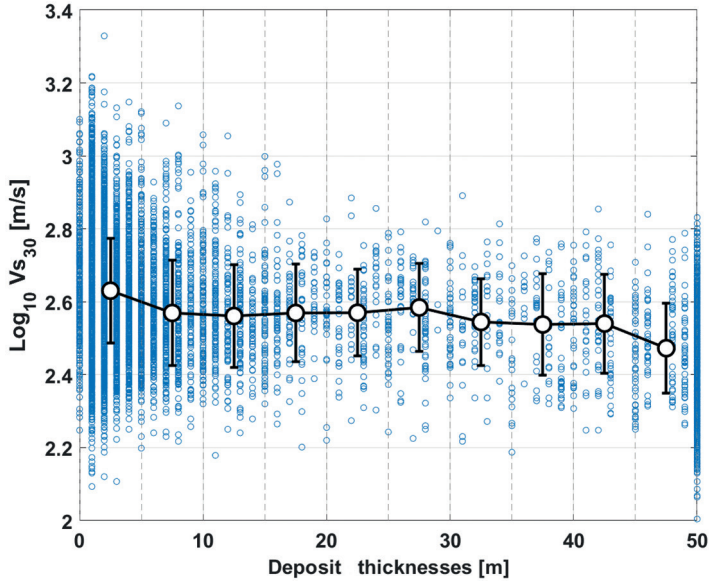

Fig. 4 - Scatter plot of $\log_{10}$(*Vs*30) versus the deposit thickness (metres) derived from Pelletier *et al*. (2016). The white markers and error bars indicate the mean and standard deviation within each bin (grey vertical dashed lines).

For the remaining numerical topographic proxies (*TRI, elevation*, *roughness*, *slope,* and *VRM*), the correlation is found to be enhanced when *Vs*30 and the numerical variable are expressed in a $\log_{10}$ scale, after replacing zero values with small positive constants. This transformation was adopted because both *Vs*30 and the morphometric proxies considered exhibit bimodal log-normal distributions; applying $\log_{10}$ reduces skewness, stabilises variance, and produces more symmetric distributions, enabling the Pearson correlation coefficient to provide a more reliable measure of association while also reducing the influence of extreme values.

Table 3 and Fig. 5 show the statistical relationships between $\log_{10}$(*Vs*30) and the numerical proxies considered expressed by the Pearson correlation coefficient. Log_{10}(*Vs*30) is positively correlated with $\log_{10}$ of five topographic indices (*TRI, elevation*, *roughness, slope,* and *VRM*) across all four spatial resolutions analysed.

Table 3 - Summary of the statistical relationships between $\log_{10}$(*Vs*30) and the numerical proxies considered. For each proxy, the table reports the Pearson correlation coefficient together with the lower and upper bounds of the 95% confidence interval (*CI*).

Proxies	Pearson *r*	95% *CI* (lower)	95% *CI* (upper)
$\log_{10}$ *TRI* 150 m	0.61	0.6	0.62
$\log_{10}$ *TRI* 250 m	0.62	0.61	0.63
$\log_{10}$ *TRI* 500 m	0.62	0.61	0.63
$\log_{10}$ *TRI* 1,000 m	0.62	0.61	0.63
$\log_{10}$ *elevation* 150 m	0.62	0.61	0.63
$\log_{10}$ *elevation* 250 m	0.62	0.61	0.63
$\log_{10}$ *elevation* 500 m	0.62	0.61	0.63
$\log_{10}$ *elevation* 1,000 m	0.62	0.61	0.63
$\log_{10}$ *roughness* 150 m	0.61	0.6	0.62
$\log_{10}$ *roughness* 250 m	0.62	0.61	0.63
$\log_{10}$ *roughness* 500 m	0.62	0.61	0.63
$\log_{10}$ *roughness* 1,000 m	0.63	0.62	0.64
$\log_{10}$ tan(*slope*) 150 m	0.6	0.59	0.61
$\log_{10}$ tan(*slope*) 250 m	0.6	0.59	0.61
$\log_{10}$ tan(*slope*) 500 m	0.6	0.59	0.61
$\log_{10}$ tan(*slope*) 1,000 m	0.61	0.59	0.62
$\log_{10}$ *VRM* 150 m	0.58	0.57	0.59
$\log_{10}$ *VRM* 250 m	0.58	0.57	0.59
$\log_{10}$ *VRM* 500 m	0.59	0.58	0.6
$\log_{10}$ *VRM* 1,000 m	0.59	0.58	0.6

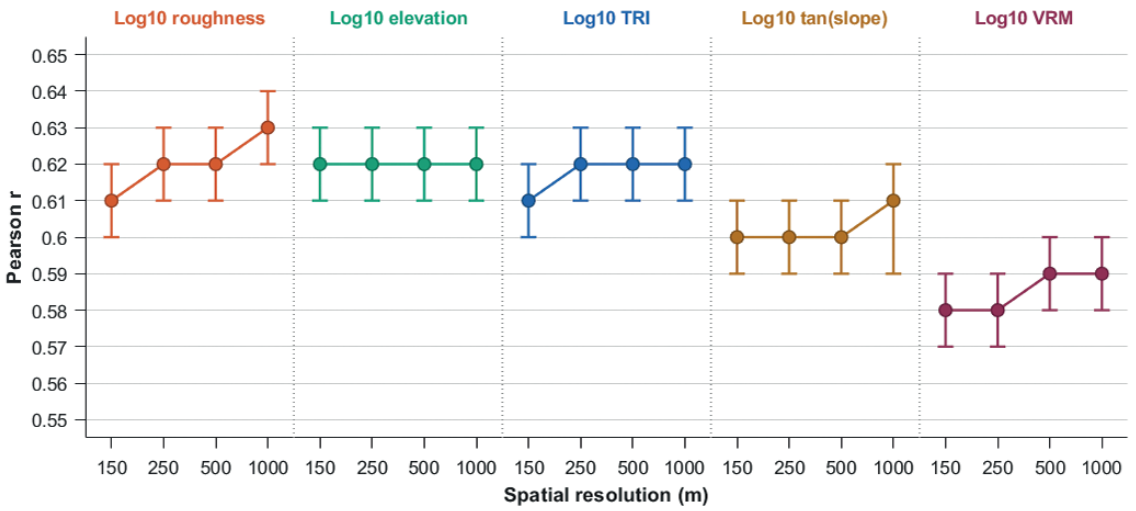

Fig. 5 - Graphical summary of the statistical relationships between $\log_{10}$(*Vs*30) and the numerical proxies considered. For each proxy and spatial resolution, the Pearson correlation coefficient (*r*) is shown together with its 95% confidence interval (*CI*).

The narrow 95% confidence intervals (CIs) indicate highly robust correlation estimates, mainly due to the large sample size. All reported correlations are associated with *p* values well below 0.01, confirming their strong statistical significance. The four topographic proxies, $\log_{10}$(*TRI*), $\log_{10}$(*elevation*), $\log_{10}$(*roughness*), and $\log_{10}$(*slope*), exhibit a similar one-dimensional trend with $\log_{10}$(*Vs*30) (see Figs. A10 to A12 and Fig. 6) and are highly correlated with one another (see Fig. A14). Log_{10}(*VRM*), instead, shows a trend with $\log_{10}$(*Vs*30) that differs from the other topographic proxies (Fig. A13).

Correlation results indicate that all log-transformed topographic proxies considered (*TRI, elevation, roughness, slope*, and *VRM*) exhibit moderate correlation with $\log_{10}$(*Vs*30), with Pearson coefficients generally ranging between about 0.58 and 0.63.

Differences among proxies are relatively small, and the corresponding 95% CIs largely overlap, indicating comparable predictive strength across the tested metrics. Considering the results across all four spatial resolutions, $\log_{10}$(*roughness)* and $\log_{10}$ (*elevation)* show the highest correlation values overall, closely followed by $\log_{10}$(*TRI)*, while $\log_{10}$ tan(*slope*) and $\log_{10}$(*VRM)* exhibit slightly lower correlations.

A slight but systematic increase in correlation with increasing spatial window size is observed for most proxies, except for *elevation*. However, the improvement is modest, typically in the order of a few hundredths in Pearson *r*. This behaviour probably reflects a reduction of small-scale topographic noise at coarser resolutions, which produces more stable terrain metrics.

Overall, these results support the use of several topographic metrics as viable candidate predictors, without indicating a single clearly dominant proxy or resolution.

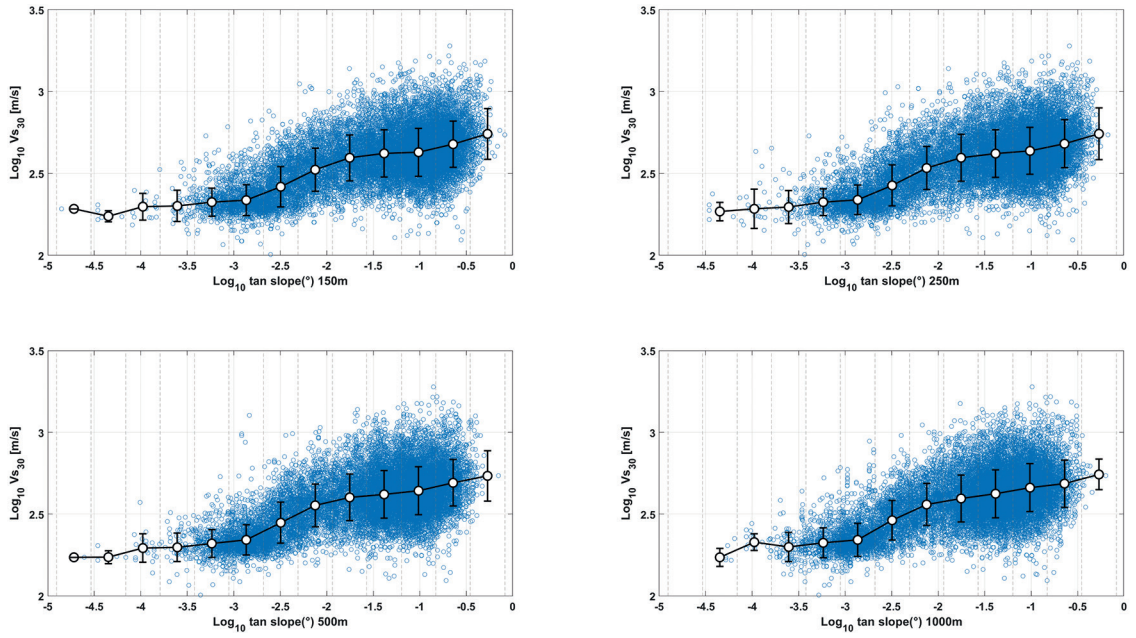

Fig. 6 - Scatter plot between $\log_{10}$(*Vs*30) [m/s] and $\log_{10}$ (*slope*) at four different resolutions. The white markers and error bars indicate the mean and standard deviation within each bin (grey vertical dashed lines).

3.2. Categorical variables

The geomorphological classification shows η² values of about 0.33 at all investigated spatial resolutions, indicating a moderate correlation with $\log_{10}$(*Vs*30). Regardless of this, it was not retained among the best proxy predictors. This decision is motivated by the fact that the largest contribution to the explained variance is attributed to the flat geomorphology class, which includes about one-fourth of the available *Vs* profiles and is separated by the rest of the classes in terms of mean *Vs*30 (Fig. 7). When the flat class is excluded, η² sharply decreases to about 0.02–0.03 across all spatial resolutions, indicating that the between-group variance component becomes very small compared to the total variance. This means that the remaining geomorphological classes have very similar mean log10(*Vs*30) values and, therefore, provide limited discriminating power.

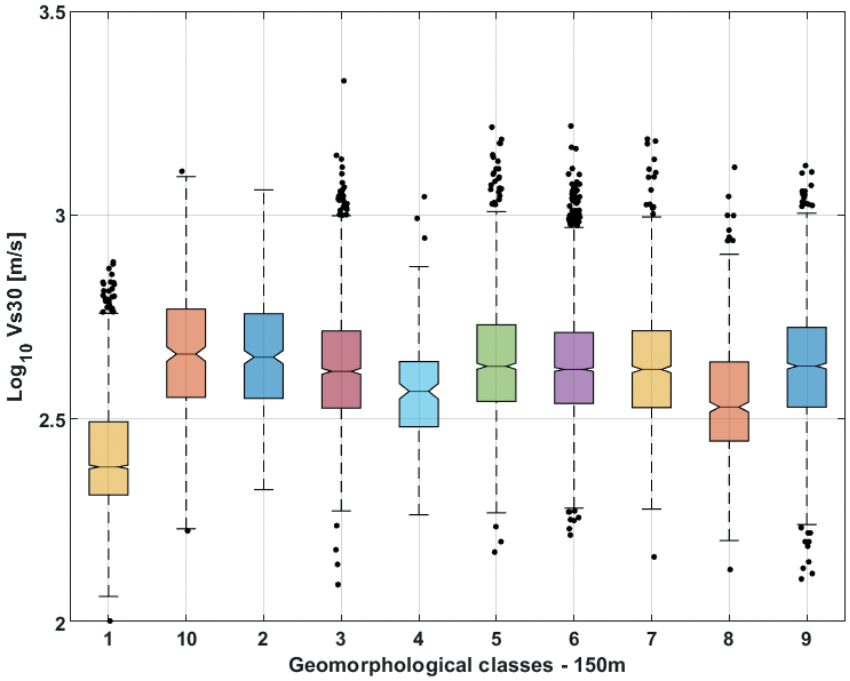

Fig. 7 - Box and whisker plot of $\log_{10}$(*Vs*30) across geomorphological classes derived from a spatial resolution of 150 m. Landform types: 1) flat, 2) peak, 3) ridge,4) shoulder, 5) spur, 6) slope, 7) hollow, 8) footslope, 9) valley, and 10) pit.

Since the η² values associated with the lithological maps proposed by ISPRA (2021) and Bucci *et al*. (2022) are 0.24 and 0.22, respectively, we performed statistical tests to evaluate the ability of different lithological classifications to explain the variability of $\log_{10}$(*Vs*30). These analyses were conducted to quantify how effectively the existing national-scale lithological maps (ISPRA, 2021; Bucci *et al*., 2022) capture the variability in $\log_{10}$(*Vs*30) and to assess whether an improved aggregation scheme could better represent this variability.

To this end, one-way Analysis of Variance (ANOVA) tests were performed between $\log_{10}$(*Vs*30) and the lithological classes proposed by ISPRA (2021) and Bucci *et al*. (2022). In the ANOVA framework, the *F*-statistic is calculated as the ratio between the variance among groups (mean square between) and the variance within groups (mean square within). A high *F*-value indicates

that the variability between groups is significantly greater than the variability within groups, suggesting that the observed differences are unlikely to be due to random chance.

The ISPRA (2021) lithological map is primarily based on lithological descriptions and geological age and includes approximately 50 classes, whereas the map proposed by Bucci *et al*. (2022) consists of 19 classes defined according to compositional and geomechanical criteria. Based on these considerations, a new lithological map was developed from the ISPRA (2021) classification by aggregating the original 50 classes using geophysical criteria to better capture the variability of $\log_{10}(Vs30)$ across different lithological groups.

To identify which lithological units of the ISPRA (2021) map could be statistically aggregated, we initially performed a pairwise Welch *t*-test (Welch, 1947) on $\log_{10}(Vs30)$ values for all possible pairs of the 50 original ISPRA lithological classes. The test was used as a preliminary screening tool to identify class pairs with statistically similar mean values. Only one lithological class, E2, has not been considered in the test, because it contains only one profile.

The original 50 ISPRA lithological classes were, then, aggregated into 11 broader groups. The aggregation was primarily guided by lithological criteria, taking into account the Welch *t*-test results on the similarity between class means. For classes represented by a limited number of measurements, grouping was mainly based on lithological criteria.

The resulting lithological grouping (Fig. 8 and Table 4) consists of:

eight classes for rocks:

- limestone and dolomites (LIDO)
- magmatic rocks and metamorphic rocks (IMR)
- effusive magmatic rocks (EMR)
- limestone-marly (LM)
- cemented and coarse sediments (CCS)
- sandstones, pelitic-arenaceous complexes, calcareous arenaceous complexes, conglomerates, travertine, quartzarenites (ARTR)
- pyroclastic rocks (PYR)
- argillites, siltstones, marls (ASM);

one class for volcanic pyroclastic deposits (PYD);

two classes for soils:

- coarse-to-medium-grained soils (SMG)
- fine grained soils (FGS).

Table 4 - Lithological codes from the new classification scheme showing the correspondence between each aggregated group and the original ISPRA (2021) lithological classes.

Lithological code	ISPRA code
CCS	A14
ARTR	A5, A8, A4, A9, A10, A15, A11
EMR	D1, D2, D3, D4
PYR	C2, D5
FGS	B1, B5
SMG	B4, B7, N1, N2, N3, A13, B2, B6, B3
PYD	D6, D8, D7
LIDO	A1, A2, G2, G3
IMR	E1, E2, E3, F1, F2, F3, F4, F5, G1, G4, G5, H1, H2
ASM	A7, C1, A12, A6
LM	A3

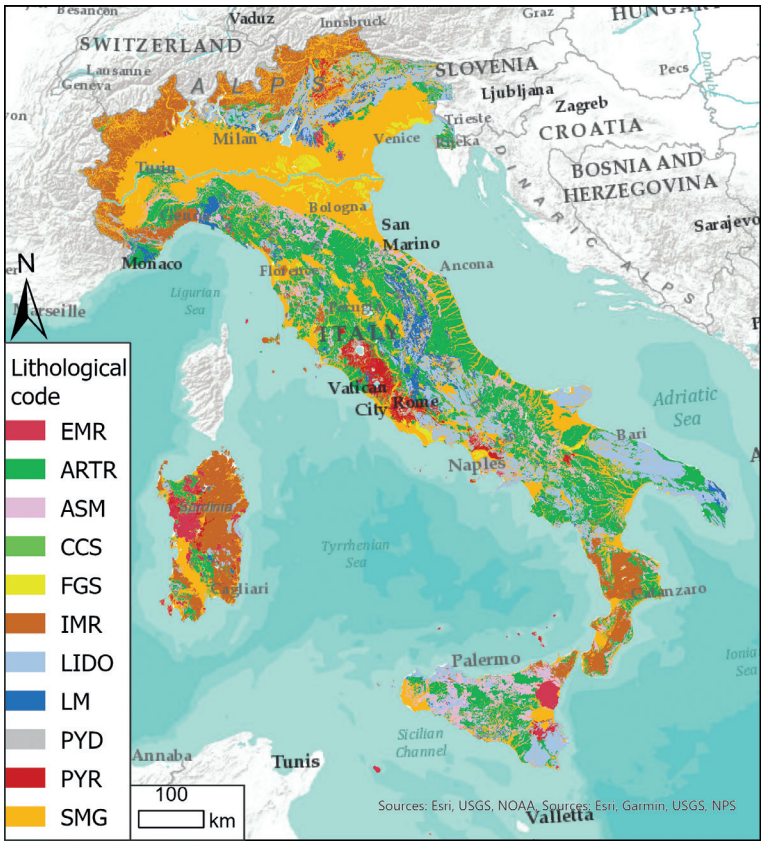

Fig. 8 - Proposed lithological classification derived from the 50 original classes of the ISPRA (2021) lithological map.

To evaluate the effectiveness of the lithological classifications in explaining $\log_{10}(Vs30)$ variability, we performed one-way ANOVA tests on the original ISPRA (2021) classification, the aggregation proposed by Bucci *et al* (2022), and the newly developed lithological classification; the *F* values (Table 5) indicate that the proposed lithological classification provides the highest level of discrimination among the three tested maps.

Table 5 - Results of the one-way ANOVA tests performed on the three lithological classifications (ISPRA, 2021; Bucci *et al.*, 2022; and the proposed classification). The table reports the *F* values and corresponding *p* values.

Lithological classification	***F* value**	***p* value**
ISPRA (2021)	125.6	< 0.05
Bucci *et al.* (2022)	244.6	< 0.05
Proposed classification	380.4	< 0.05

Specifically, the ANOVA applied to the new lithological classification yields an *F* value of 380.4 with a *p* value lower than 0.05 (Fig. 9), indicating that the variability of $\log_{10}(Vs30)$ between lithological classes is substantially greater than the variability within the classes. This *F* value is significantly higher than the values obtained for the classification proposed by Bucci *et al*. (2022) ($F = 244.6$, $p < 0.05$) and for the original ISPRA (2021) classification ($F = 125.6$, $p < 0.05$).

Although all three lithological groupings show statistically significant relationships with $\log_{10}(Vs30)$, the higher *F* values indicate that the newly defined lithological classes capture the variability in $\log_{10}(Vs30)$ more effectively, providing a more robust basis for future regression analyses and large-scale *Vs*30 mapping.

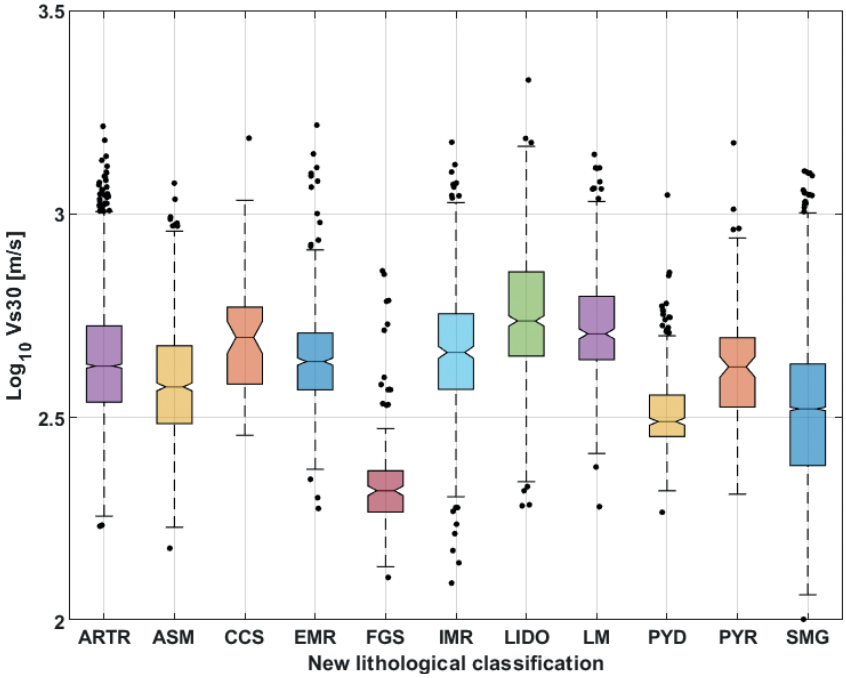

Fig. 9 - Box and whisker plot showing the variability of $\log_{10}(Vs30)$ across the new lithological classification.

4. Discussion and conclusions

This study has focused on evaluating the predictive capability of lithological and geomorphological proxies for shear-wave velocity in the uppermost 30 m (*Vs*30) in Italy. We compiled a dataset of approximately 15,000 shear-wave velocity profiles, evenly distributed across the Italian territory and examined the availability of existing nationwide proxies for *Vs*30 with the long-term goal of calibrating a *Vs*30 map.

Two lithological maps, both ultimately derived from the 1:100,000 geological map of Italy, are available (ISPRA, 2020). The first is the map released by ISPRA (2021), which classifies the geological units into 50 lithological classes. The second is the alternative map proposed by Bucci *et al*. (2022), which reclassifies the original geological units into 19 categories according to compositional and geomechanical criteria.

We selected the 10 m × 10 m DEM by Tarquini *et al*. (2023) and calculated 10 topographic indices at four different resolutions (150 m, 250 m, 500 m, and 1,000 m). Additionally, we considered the soil thickness map by Pellettieri *et al*. (2016), which is globally calibrated at a resolution of approximately 1 km².

Our results indicate that $\log_{10}(Vs30)$ is positively correlated with the $\log_{10}$ of five topographic indices (*TRI, elevation, roughness, slope* expressed as the tangent of the slope angle, and *VRM*) across all four spatial resolutions analysed, with Pearson coefficients generally between about

0.58 and 0.63. In contrast, sediment thickness derived from the global dataset of Pelletier *et al*. (2016) shows a moderate negative correlation with $\log_{10}$(*Vs*30), although the *Vs*30 observations are predominantly clustered within two thickness intervals (0–15m and > 50 m).

The correlation of topographic proxies (*TRI, elevation, roughness, slope,* and *VRM*) with *Vs*30 have 95% CIs which largely overlap, indicating comparable predictive strength. Across the four tested spatial resolutions, $\log_{10}$(*roughness*) and $\log_{10}$(*elevation*) show the highest correlations with $\log_{10}$(*Vs*30), closely followed by $\log_{10}$(*TRI*), whereas $\log_{10}$ tan(*slope*) and $\log_{10}$(*VRM*) yield slightly lower values. A small increase in correlation is observed at coarser spatial windows (except for *elevation*), typically limited to a few hundredths in Pearson *r*. This trend is consistent with the findings of Allen and Wald (2009) for *slope*–*Vs*30 relationships and likely reflects the reduction of small-scale topographic noise at coarser resolutions, leading to more stable terrain metrics. Moreover, since a substantial proportion of *Vs* profiles are in flat areas characterised by low topographic variability, resampling the raster to coarser resolutions produces only minor changes in the derived terrain metrics, thereby preserving the overall correlation pattern.

TPI, standard, planform, and *profile curvature* show only weak linear correlations with $\log_{10}$(*Vs*30) ($|r| \leq 0.15$ at all tested resolutions) and were, therefore not considered as suitable predictors. The geomorphological classification shows moderate η^2 values (about 0.33), but this effect is mainly driven by the "flat" class; excluding it, η^2 reduces to about 0.02–0.03, highlighting the limited explanatory power of the remaining classes.

Finally, we calibrated a *Vs*30-oriented lithological map derived from the original ISPRA (2021) map by aggregating the 50 initial classes into 11 broader groups, primarily based on lithological criteria and supported by statistical screening of differences in mean $\log_{10}$(*Vs*30) values.

The proxies identified will be used to calibrate a preliminary nationwide *Vs*30 model (Brunelli, 2025), although we acknowledge several limitations. First, the absence of *Vs* profiles in rock units, since geophysical tests are generally performed on soils. Moreover, the use of a more detailed geological map, such as the nationwide 1:50,000 scale, could improve the detection of smaller soil units, although this map is not yet available for the entire country.

The ongoing availability of new data, including *Vs* profiles, geological maps, and seismological studies, renders the development of a *Vs*30 model highly dynamic. Such a model would necessitate the coordinated efforts of academic researchers and industry to ensure its accuracy and adaptability.

Acknowledgments. The authors are grateful to Oliver S. Boyd for his valuable suggestions, which significantly contributed to the improvement of this work. We also thank Charles Bruce Worden for the valuable discussions and insights shared during the research phase. The authors thank the reviewers for their constructive comments, which helped to improve the manuscript. Any use of trade, firm, or product names is for descriptive purposes only and does not imply endorsement by the U.S. Government.

REFERENCES

Abrahamson N. and Silva W.; 2008: *Summary of the Abrahamson and Silva NGA ground-motion relations*. Earthquake Spectra, 24(1), 67–97, doi: 10.1193/1.2924360.

Aki K.; 1957: *Space and time spectra of stationary stochastic waves, with special reference to microtremors.* Bull. Earthquake Res. Inst., 35, 415–456.

Aki, K.; 1988: *Local site effects on ground motion.* In: Von Thun J.L. (ed), Earthquake engineering and soil dynamics II Recent advances in ground-motion evaluation, Am. Soc. Civil Eng., Geotechnical Special Publication No. 20, Amer. Society of Civil Engineers, Park City, UT, USA, pp. 103-155.

Allen T.I. and Wald D.J.; 2009: *On the use of high-resolution topographic data as a proxy for seismic site conditions (V_{S30}).* Bull. Seismol. Soc. Am., 99, no. 2A, 935–943, doi: 10.1785/0120080255.

Asten M.W.; 2006: *On bias and noise in passive seismic data from finite circular array data processed using SPAC methods.* Geophysics, 71(6), V153–V162, doi: 10.1190/1.2345054.

Bonomo R., Capotorti F., D'Ambrogi C., Di Stefano R., Graziano R., Martarelli L., Pampaloni M.L., Pantaloni M., Ricci V., Compagnoni B., Galluzzo F., Tacchia D., Masell G., Pannuti V., Ventura R. and Vitale V.; 2005: *Carta geologica d'Italia alla scala 1:1250000*. Servizio Geologico d'Italia, APAT, Roma.

Boore D.M., Joyner W.B. and Fumal T.E.; 1997: *Equations for estimating horizontal response spectra and peak acceleration from western north American earthquakes: a summary of recent work*. Seismol. Res. Lett., 68(1), 128–153, doi: 10.1785/gssrl.68.1.128.

Boore D.M. and Atkinson G.M.; 2008: *Ground-motion prediction equations for the average horizontal component of PGA, PGV, and 5%-damped PSA at spectral periods between 0.01 s and 10.0 s.* Earthquake Spectra, 24(1), 99–138, doi: 10.1193/1.2830434.

Borcherdt R.D. and Glassmoyer G.; 1995 *Influences of local geology on strong and weak ground motions recorded in the San Francisco Bay region and their implications for site-specific building-code provisions.* International J. of Rock Mechanics and Mining Sciences and Geomechanics Abstracts, 32, A77-A108, doi: 10.1016/0148-9062(95)99404-L.

Brunelli G.; 2025: *Calibration of correction factors for source, attenuation and site effects to predict ground shaking across Italy.* Università di Camerino, Doctoral thesis, https://hdl.handle.net/11581/498511.

Bucci F., Santangelo M., Fongo L., Alvioli M., Cardinali M., Melelli L. and Marchesini I.; 2021: *A new digital lithological Map of Italy at 1:100,000 scale [dataset].* PANGAEA, doi: 10.1594/PANGAEA.935673.

Bucci F., Santangelo M., Fongo L., Alvioli M., Cardinali M., Melelli L. and Marchesini I.; 2022: *A new digital lithological map of Italy at the 1:100,000 scale for geomechanical modelling.* Earth Syst. Sci. Data, 14(9), 4129–4151, doi: 10.5194/essd-14-4129-2022.

Campbell K.W. and Bozorgnia Y.; 2008: *NGA ground motion model for the geometric mean horizontal component of PGA, PGV, PGD and 5% damped linear elastic response spectra for periods ranging from 0.01 to 10 s.* Earthquake Spectra, 24(1), 139–171, doi: 10.1193/1.2857546.

CEN; 2004: *Eurocode 8: Design of structures for earthquake resistance– Part 1: General rules, seismic actions and rules for buildings*. European Committee for Standardization, Brussels, Belgium, 229 pp.

Chiou B.S.-J. and Youngs R.R.; 2014: *Update of the Chiou and Youngs NGA model for the average horizontal component of peak ground motion and response spectra.* Earthquake Spectra, 30(3), 1117–1153, doi: 10.1193/072813EQS219M.

Choi J., Stewart J.P., Buckreis T.E. and Brandenberg S.J.; 2025: Proxy-based VS30 estimation for Utah conditioned on surface geology and surface gradient. In: Montgomery J. and Cox B.R. (eds), Geo-Congress 2026: Earthquake Engineering and Soil Dynamics, 9-12 March 2026, Salt Lake City, Utah, USA, doi. org/10.1061/9780784486702.0.

Cipolloni C., Pantaloni M., Ventura R., Vitale V. and Tacchia D.; 2009: *The GEO1MDB: the database of the 1:1,000,000 scale Geological Map of Italy. In:* 6th EUREGEO, European Congress on Regional Geoscientific Cartography and Information Systems, Munich, Bavaria, Germany, 9–12 June 2009, pp. 215–217.

Compagnoni B.; 2004: *La Carta geologica d'Italia, alla scala 1:1,000,000.* Mem. Descr. Carta Geol. It., 71, 207–212.

Compagnoni B., Damiani A.V. and Valletta M.; 1976–1983: *Carta geologica d'Italia alla scala 1:500,000.* In 5 fogli e note illustrative, Servizio Geologico d'Italia, Roma.

Crespo M.J., Benjumea B., Moratalla J.M., Lacoma L., Macau A., González Á., Gutiérrez F. and Stafford P.J.; 2022: *A proxy-based model for estimating V_{S30} in the Iberian Peninsula.* Soil Dyn. Earthquake Eng., 155, 107165, doi: 10.1016/j.soildyn.2022.107165.

Cultrera G. and Mercuri A.; 2025: *Statistical analysis of site effect indicators at the Italian seismic network: inside the site characterization database CRISP*. Bull. Earthquake Eng., 23(11), 4365–4390, doi: 10.1007/s10518-025-02212-y.

Delogu D., Campo V., Cipolloni C., Congi M.P., Falcetti S., Moretti P., Pampaloni M.L., Pantaloni M., Roma M. and Ventura R.; 2012: *Il Portale del Servizio Geologico d'Italia: uno strumento al servizio dei geologi professionisti.* Professione Geologo, 32, 24–27.

EPOS (European Plate Observing System); n.d.: *European Plate Observing System*. https://www.epos-eu.org.

Esri Inc.; 2024: *ArcGIS Pro, Version 3.4.2.* Environmental Systems Research Institute Inc., Redlands, CA, USA, https://pro.arcgis.com/en/pro-app/latest/get-started/download-arcgis-pro.htm.

Felicetta C., Russo E., D'Amico M., Sgobba S., Lanzano G., Mascandola C., Pacor F. and Luzi L.; 2023: *Italian Accelerometric Archive (ITACA), version 4.0*. Istituto Nazionale di Geofisica e Vulcanologia (INGV), doi: 10.13127/itaca.4.0.

Field E.H.; 2000: *A modified ground-motion attenuation relationship for southern California that accounts for detailed site classification and a basin-depth effect.* Bull. Seismol. Soc. Am., 90(6B), S209–S221, doi: 10.1785/0120000507.

Fisher R.A.; 1925: *Statistical methods for research workers.* Oliver and Boyd ed., Edinburgh, United Kingdom, 339 pp.

Forte G., Chioccarelli E., De Falco M., Cito P., Santo A. and Iervolino I.; 2019: *Seismic soil classification of Italy based on surface geology and shear-wave velocity measurements.* Soil Dyn. Earthquake Eng., 122, 79–93, doi: 10.1016/j.soildyn.2019.04.002.

Foster K.M., Bradley B.A., McGann C.R. and Wotherspoon L.M.; 2019: *A V_{S30} map for New Zealand based on geologic and terrain proxy variables and field measurements.* Earthquake Spectra, 35(4), 1865–1897, doi: 10.1193/121118EQS281M.

GDAL Development Team; 2021. *GDAL – Geospatial Data Abstraction Library, Version 3.4*. Open Source Geospatial Foundation, https://gdal.org, accessed 25 September 2025.

Geyin M. and Maurer B.W.; 2023: *U.S. national V_{S30} models and maps informed by remote sensing and machine learning*. Seismol. Res. Letters, 94(3), 1467–1477, doi: 10.1785/0220220181.

Gironelli V., Volatili T., Luzi L., Brunelli G. and Tondi E; 2024: *Dual-proxy estimation of Vs30.* the case study of the Marche Region (central Italy). J. of Maps, 20(1), 2349787, doi: 10.1080/17445647.2024.2349787.

Hobson R.D.; 1972: *Surface roughness in topography: a quantitative approach.* In: Chorley R.J. (ed), Spatial Analysis in Geomorphology, Methuen and Co., London, pp. 221–245.

Hough S.E., Friberg P.A., Busby R., Field E.F., Jacob K.H. and Borcherdt R.D.; 1990: *Sediment-induced amplification and the collapse of the Nimitz Freeway*. Nature, 344, 853-855, doi: 10.1038/344853a0.

INGV Sezione di Pisa: n.d.: Surflt. https://tinitaly.pi.ingv.it.

ISPRA; 2020: *Geological Map of Italy at 1:100,000 scale.* https://inspire-geoportal.ec.europa.eu/srv/ita/catalog.search#/metadata/ispra_rm:Geologia100K_DT, accessed 25 May 2026.

ISPRA; 2021: *Lithological map of Italy at 1:100,000 scale.* https://inspire-geoportal.ec.europa.eu/srv/ita/catalog.search#/metadata/ispra_rm:Meta_Geo_SV000004_SVD.

Jasiewicz J. and Stepinski T.F.; 2013: *Geomorphons - a pattern recognition approach to classification and mapping of landforms.* Geomorphology, 182, 147–156, doi: 10.1016/j.geomorph.2012.11.005.

Lanzano G., Luzi L., Pacor F., Felicetta C., Puglia R., Sgobba S. and D'Amico M.; 2019: *A revised ground-motion prediction model for shallow crustal earthquakes in Italy.* Bull. Seismol. Soc. Am., 109(2), 525–540, doi: 10.1785/0120180210.

Lee V.W. and Trifunac M.D.; 2010: *Should average shear-wave velocity in the top 30 m of soil be used to describe seismic amplification?* Soil Dyn. Earthquake Engin., 30, 1250-1258.

Louie J.N.; 2001: *Faster, better: shear-wave velocity to 100 meters depth from refraction microtremor arrays.* Bull. Seismol. Soc. Am., 91(2), 347–364, doi: 10.1785/0120000098.

Loviknes K., Cotton F. and Weatherill G.; 2024: *Exploring inferred geomorphological sediment thickness as a new site proxy to predict ground-shaking amplification at regional scale: application to Europe and eastern Türkiye.* Nat. Hazards Earth Syst. Sci., 24(4), 1223–1247, doi: 10.5194/nhess-24-1223-2024.

Luzi L., Pacor F., Ameri G., Puglia R., Burrato P., Massa M., Augliera P., Franceschina G., Lovati S. and Castro R.; 2013: *Overview on the strong-motion data recorded during the May–June 2012 Emilia seismic sequence.* Seismol. Res. Lett., 84(4), 629–644, doi: 10.1785/0220120154.

Martin G.R. and Dobry R.; 1994: *Earthquake site response and seismic code provisions.* In: U.S. National Center for Earthquake Engineering Research (NCEER). Research accomplisments : 1986 - 1994. Buffalo, N.Y, U.S. National Center for Earthquake Engineering Research (NCEER), pp.121-30.

MIT (Ministero delle Infrastrutture e dei Trasporti); 2018: *Decreto 17 gennaio 2018. Aggiornamento delle "Norme Tecniche per le Costruzioni"*. Gazzetta Ufficiale, 42, 20-02-2018, Supplemento Ordinario n. 8, https://www.bosettiegatti.eu/info/norme/statali/2018_dm_17_01_norme_tecniche.pdf.

Moore I.D., Grayson R.B. and Ladson A.R.; 1991: *Digital terrain modelling: a review of hydrological, geomorphological, and biological applications.* Hydrological processes, 5(1), 3-30, doi: 10.1002/hyp.3360050103.

Mori F., Mendicelli A., Moscatelli M., Romagnoli G., Peronace E. and Naso G.; 2020: *A new Vs30 map for Italy based on the seismic microzonation dataset.* Eng. Geol., 275, 105745, doi: 10.1016/j.enggeo.2020.105745.

Mori F., Naso G., Mendicelli A. and Ciotoli G.; 2026: *Machine learning-based national Vs_{30} models and maps for Italy*. Soil Dyn. Earthquake Eng., 203, 110077, doi: 10.1016/j.soildyn.2025.110077.

Navarro M., López F., Martínez-Pagán P., García-Jerez A., Martínez-Segura M.A., Oda Y. and Enomoto T.; 2025: *Estimating VS_{30} structure from topographic and geological data in the southeast of Spain*. Eng. Geol., 351, 108037, doi: 10.1016/j.enggeo.2025.108037.

Pantaloni M.; 2011: *La Carta geologica d'Italia alla scala 1:1,000,000: una pietra miliare nel percorso della conoscenza geologica*. Geologia Tecnica and Ambientale, 11, 88–99.

Paolucci E., Cavuoto G., Cosentino G., Coltella M., Simionato M., Cavinato G.P., Trulli I. and Albarello D.; 2021: *Regional seismic characterization of shallow subsoil of northern Apulia (southern Italy)*. Geosci., 11(10), 416, doi: 10.3390/geosciences11100416.

Park C.B., Miller R.D. and Xia J.; 1999: *Multichannel analysis of surface waves.* Geophys., 64(3), 800–808, doi: 10.1190/1.1444590.

Parker G.A., Harmon J.A., Stewart J.P., Hashash Y.M., Kottke A.R., Rathje, E.M. Silva, W.J. and Campbell K.W.; 2017: *Proxy-based VS30 estimation in central and eastern North America.* Bull. Seismol. Soc. Am., 107, 117-131.

Pearson K.; 1895: *VII. Note on regression and inheritance in the case of two parents*. Proceedings of the Royal Soc. of London, 58(347-352), 240–242, doi: 10.1098/rspl.1895.0041.

Pelletier J.D., Broxton P.D., Hazenberg P., Zeng X., Troch P.A., Niu G-Y., Williams Z., Brunke M.A. and Gochis D.; 2016: *A gridded global data set of soil, intact regolith, and sedimentary deposit thicknesses for regional and global land surface modeling.* J. of Advances in Modeling Earth Systems, 8(1), 41–65, doi: 10.1002/2015MS000526.

Perrin N.D., Heron D., Kaiser A. and Van Houtte C.; 2015: *V_S30 and NZS 1170.5 site class maps of New Zealand* . In: Proceedings of 2015 New Zealand Society for Earthquake Engineering Technical Conference, Rotorua, 10-12 April, Paper O-07, https://pdfs.semanticscholar.org/1565/22c77778c7a67d58139746e71852a50d3f02.pdf.

Pitilakis. K., Riga E., Anastasiadis A., Fotopoulou S. and Karafagka S.; 2019: *Towards the revision of EC8: proposal for an alternative site classification scheme and associated intensity dependent spectral amplification factors.* Soil Dyn. Earthquake Engin., 126, 105137.

Puglia R., Vona M., Klin P., Ladina C., Masi A., Priolo E. and Silvestri F.; 2013: *Analysis of site response and building damage distribution induced by the 31 October 2002 earthquake at San Giuliano di Puglia (Italy).* Earthquake Spectra, 29(2), 497–526, doi: 10.1193/1.4000134.

QGIS Development Team; 2022: *QGIS Geographic Information System, Version 3.22.11*. Open Source Geospatial Foundation Project, https://qgis.org, accessed 25 September 2025.

Riley S.J., DeGloria S.D. and Elliot R; 1999: *A terrain ruggedness index that quantifies topographic heterogeneity.* Intermountain J. of Sciences, 5(1-4), 23–27.

Safani J., O'Neill A., Matsuoka T. and Sanada Y.; 2005: *Applications of Love wave dispersion for improved shear-wave velocity imaging.* J. Environ. Eng. Geophys., 10(2), 135–150, doi: 10.2113/JEEG10.2.135.

Sappington J.M., Longshore K.M. and Thompson D.B.; 2007: *Quantifying landscape ruggedness for animal habitat analysis: a case study using bighorn sheep in the Mojave Desert.* J. of Wildlife Management, 71(5), 1419–1426, doi: 10.2193/2005-723.

Singh S.K. and Ordaz M.; 1993: *On the origin of long coda observed in the lake-bed strong-motion records of Mexico City*. Bull. Seismol. Soc. Am., 83(4), 1298–1306, doi: 10.1785/BSSA0830041298.

Spudich P., Hellweg M. and Lee W.H.K.; 1996: *Directional topographic site response at Tarzana observed in aftershocks of the 1994 Northridge, California, earthquake: implications for mainshock motions.* Bull. Seismol. Soc. Am., 86(1B), S193–S208, doi: 10.1785/BSSA08601BS193.

Stephenson W.J., Hartzell S., Frankel A.D., Asten M., Carver D.L. and Kim, W.Y.; 2009: *Site characterization for urban seismic hazards in lower Manhattan, New York City, from microtremor array analysis.* Geophys. Res. Lett., 36(3), L03301, doi: 10.1029/2008GL036444..

Stewart J.P., Klimis N, Savvaidis A, Theodoulidis N, Zargli E, Athanasopoulos G, Pelekis P, Mylonakis G. and Margaris B., 2014: *Compilation of a local V_S profile database and its application for inference of V_{S30} from geologic-and terrain-based proxies*. Bull. Seismol. Soc. Am., 104(6), 2827–2841, doi: 10.1785/0120130331.

Strollo A., Richwalski S.M., Parolai S., Gallipoli M.R., Mucciarelli M. and Caputo R.; 2007: *Site effects of the 2002 Molise earthquake, Italy: analysis of strong motion, ambient noise, and synthetic data from 2D modelling in San Giuliano di Puglia.* Bull. Earthquake Eng., 5, 347–362, doi: 10.1007/s10518-007-9033-6.

Tarquini S., Isola I., Favalli M., Battistini A. and Dotta G.; 2023: *TINITALY, a digital elevation model of Italy with a 10 meters cell size (Version 1.1)*. Istituto Nazionale di Geofisica e Vulcanologia (INGV), doi: 10.13127/tinitaly/1.1.

Tertulliani A., Leschiutta I., Bordoni P. and Milana G.; 2012: *Damage distribution in L'Aquila city (central Italy) during the 6 April 2009 earthquake.* Bull. Seismol. Soc. Am., 102(4), 1543–1553, doi: 10.1785/0120110205.

Thompson E.M., Wald D.J. and Worden C.B.; 2014: *A V_{S30} map for California with geologic and topographic constraints.* Bull. Seismol. Soc. Am.,, 104(5), 2313–2321, doi: 10.1785/0120130312.

Wald D.J. and Allen T.I.; 2007: *Topographic slope as a proxy for seismic site conditions and amplification*. Bull. Seismol. Soc. Am., 97(5), 1379–1395, doi: 10.1785/0120060267.

Wakamatsu K. and Matsuoka M.; 2011: *Developing a 7.5-sec site-condition map for Japan based on geomorphologic classification.* In: Brebbia C.A. and Maugeri M. (eds), Earthquake Resistant Engineering Structures VIII, WIT Press, Southampton, UK, pp. 101–112.

Web MS-CLE (Portale cartografico della Microzonazione Sismica e della Condizione Limite per l'Emergenza); n.d.: *Sistema Web-GIS*. https://www.webms.it/servizi/viewer.php.

Weiss A.; 2001: *Topographic position and landforms analysis.* In: Poster presentation, ESRI user conference, San Diego, CA, USA, Vol. 200, https://env761.github.io/assets/files/tpi-poster-tnc_18x22.pdf.

Welch B.L.; 1947: *The generalization of 'Student's' problem when several different population variances are involved.* Biometrika, 34(1-2), 28–35, doi: 10.2307/2332510.

Wills C.J., Gutierrez C.I., Perez F.G. and Branum D.M.; 2015: *A next generation V_{S30} map for California based on geology and topography.* Bull. Seismol. Soc. Am., 105(6), 3083–3091, doi: 10.1785/0120150105.

Wilson M.F., O'Connell B., Brown C., Guinan J.C. and Grehan A.J.; 2007: *Multiscale terrain analysis of multibeam bathymetry data for habitat mapping on the continental slope*. Mar. Geodesy, 30(1-2), 3–35, doi: 10.1080/01490410701295962.

Yong A., Hough S.E., Iwahashi J. and Braverman A.; 2012: *A terrain-based site-conditions map of California with implications for the contiguous United States*. Bull. Seismol. Soc. Am., 102(1), 114–128, doi: 10.1785/0120100262.

Yong A., Thompson E., Wald D.J., Knudsen K.L., Odum J.K., Stephenson W.J. and Haefner S.; 2016: *Compilation of V_{S30} data for the United States*. U.S. Geol. Surv. Data Series 978, Report: iii, 8 pp.; Appendix, doi: 10.3133/ds978.

Zevenbergen L.W. and Thorne C.R.; 1987: *Quantitative analysis of land surface topography*. Earth Surface Processes and Landforms, 12(1), 47–56, doi: 10.1002/esp.3290120107.

Corresponding author: Giulio Brunelli
Istituto Nazionale di Geofisica e Vulcanologia, Sezione di Milano
Via Alfonso Corti 12, Milano, Italy
Phone: +39 3402407968; e-mail: giulio.brunelli@ingv.it

Appendix A

Fig. A1 - *TRI* map calculated with a spatial resolution of 150 m. The raster has a minimum value of 0, a maximum value of 6,768 m, and an average value of 78 m.

Fig. A2 - *VRM* map calculated with a spatial resolution of 150 m. The raster has a minimum value of 0, a maximum value of 0.4, and an average value of 0.006.

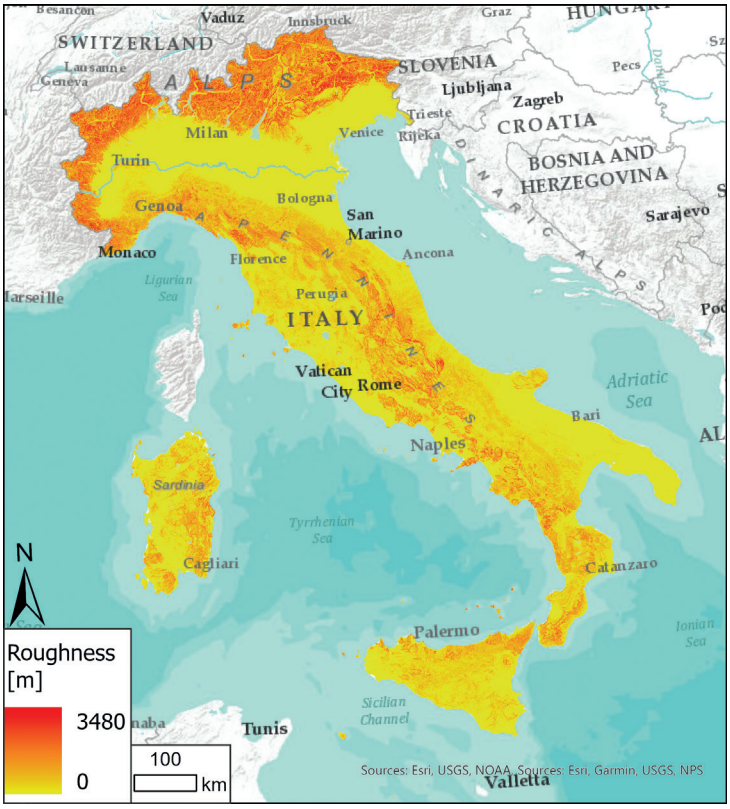

Fig. A3 - *Roughness* map calculated with a spatial resolution of 150 m. The raster has a minimum value of 0, a maximum value of 3,480, and an average value of 74.

Fig. A4 – *TPI* map calculated with a spatial resolution of 150 m. The raster has a minimum value of -1,691 m, a maximum value of 1,265 m, and an average value of 2.52 m.

Fig. A5 - *Profile curvature* map calculated with a spatial resolution of 150 m. The raster has a minimum value of -15.8×10^{-2} m^{-1}, a maximum value of 15.2×10^{-2} m^{-1}, an average value of 0.005×10^{-2} m^{-1}, and a standard deviation of 0.13×10^{-2} m^{-1}.

Fig. A6 - *Plan curvature* map calculated with a spatial resolution of 150 m. The raster has a minimum value of -14.8×10⁻² m⁻¹, a maximum value of 5.4×10⁻² m⁻¹, an average value of 0.005×10⁻² m⁻¹, and a standard deviation of 0.15×10⁻² m⁻¹.

Fig. A7 - *Standard curvature* map calculated with a spatial resolution of 150 m. The raster has a minimum value of -30×10⁻² m⁻¹, a maximum value of 15.3×10⁻² m⁻¹, an average value close to zero, and a standard deviation of 0.25×10⁻² m⁻¹.

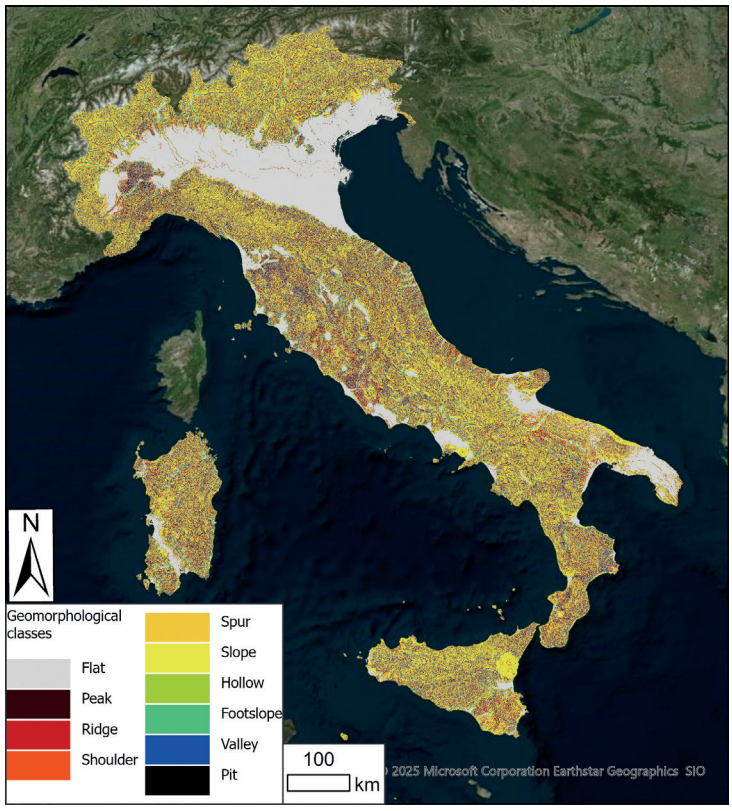

Fig. A8 - Geomorphological class map calculated with a spatial resolution of 150 m.

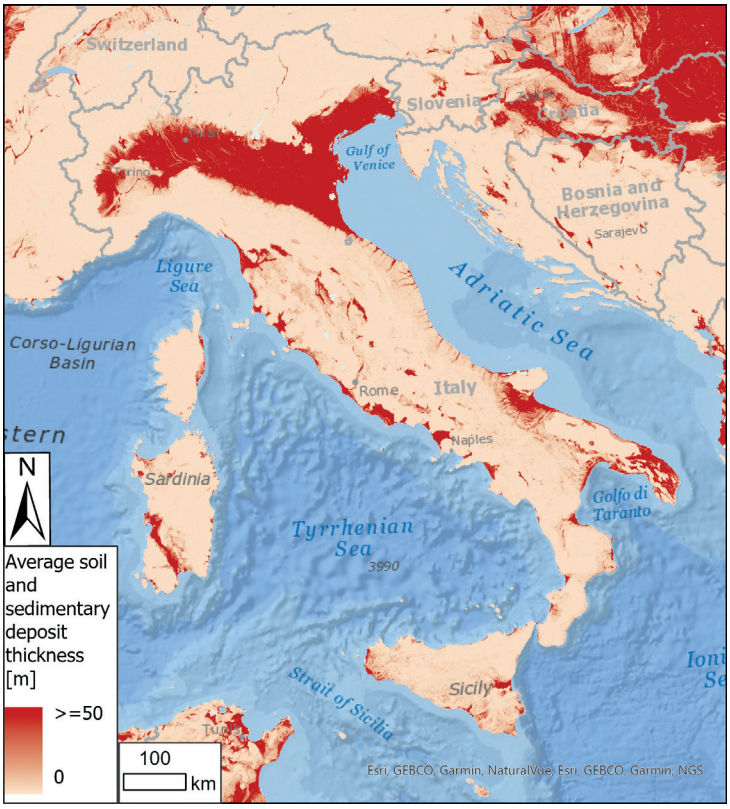

Fig. A9 - Average soil and sedimentary deposit thickness [m] map as proposed by Pelletier *et al*. (2016).

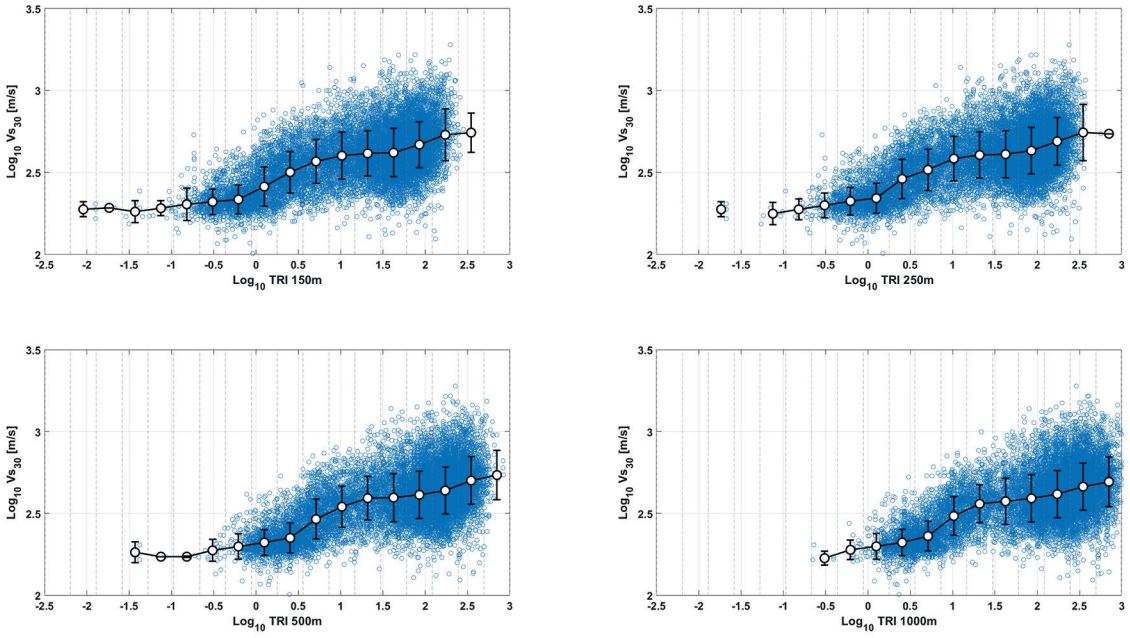

Fig. A10 - Scatter plot between $\log_{10}$*Vs*30 [m/s] and $\log_{10}$ (*TRI*). The white markers and error bars indicate the mean and standard deviation within each bin (grey vertical dashed lines).

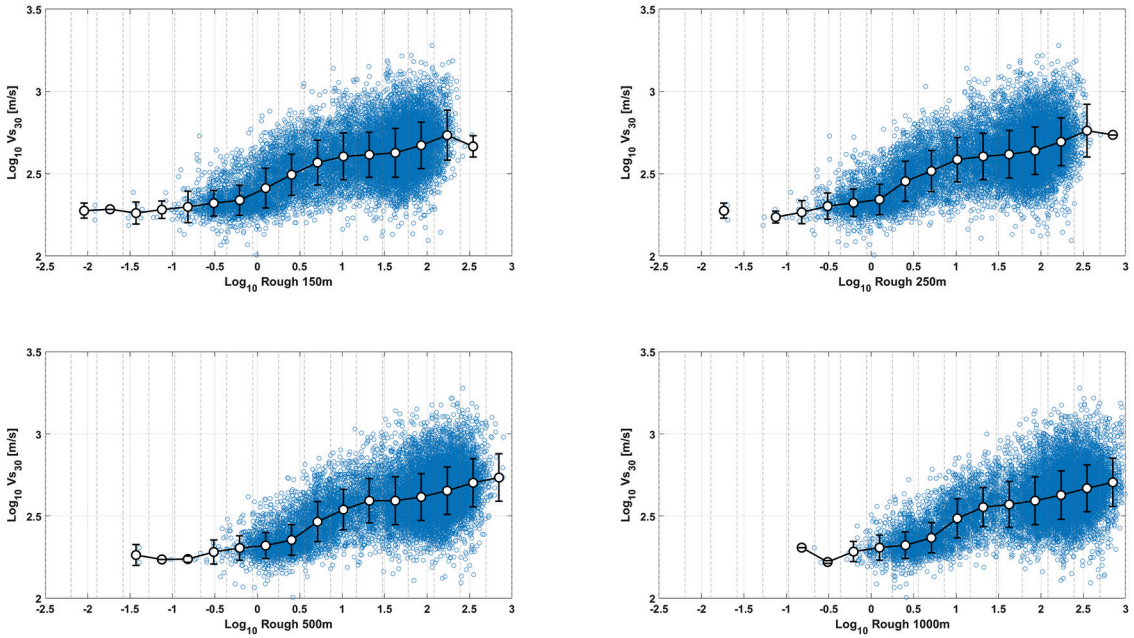

Fig. A11 - Scatter plot between $\log_{10}$*Vs*30 [m/s] and $\log_{10}$(*roughness*). The white markers and error bars indicate the mean and standard deviation within each bin (grey vertical dashed lines).

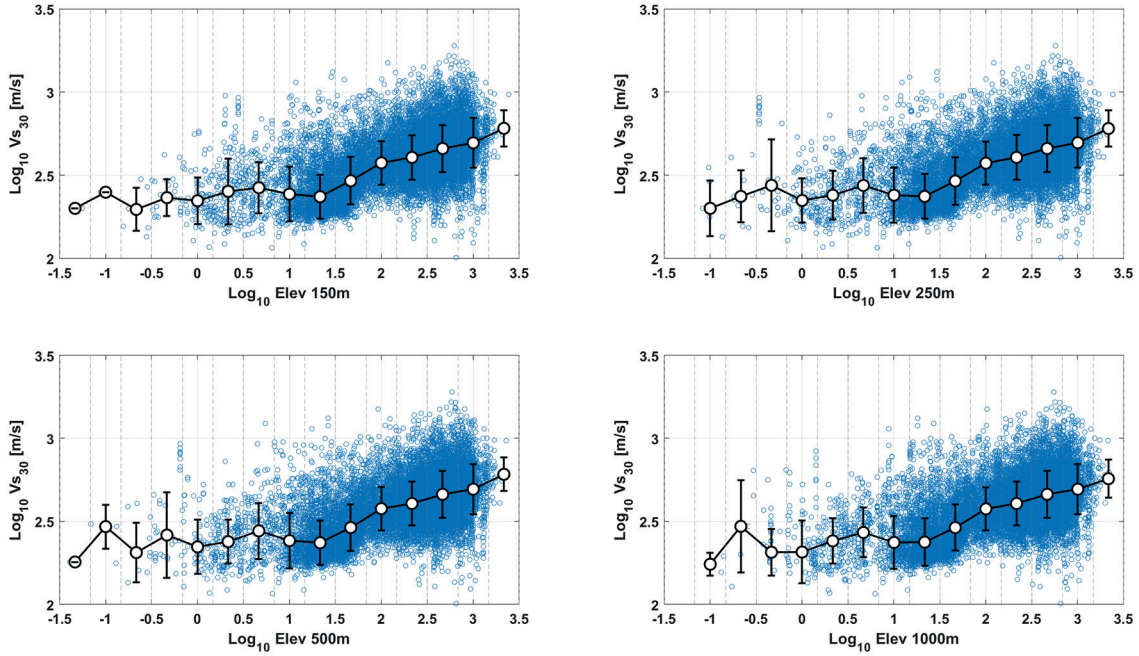

Fig. A12 - Scatter plot between $\log_{10}$*Vs*30 [m/s] and $\log_{10}$(*elevation*). The white markers and error bars indicate the mean and standard deviation within each bin (grey vertical dashed lines).

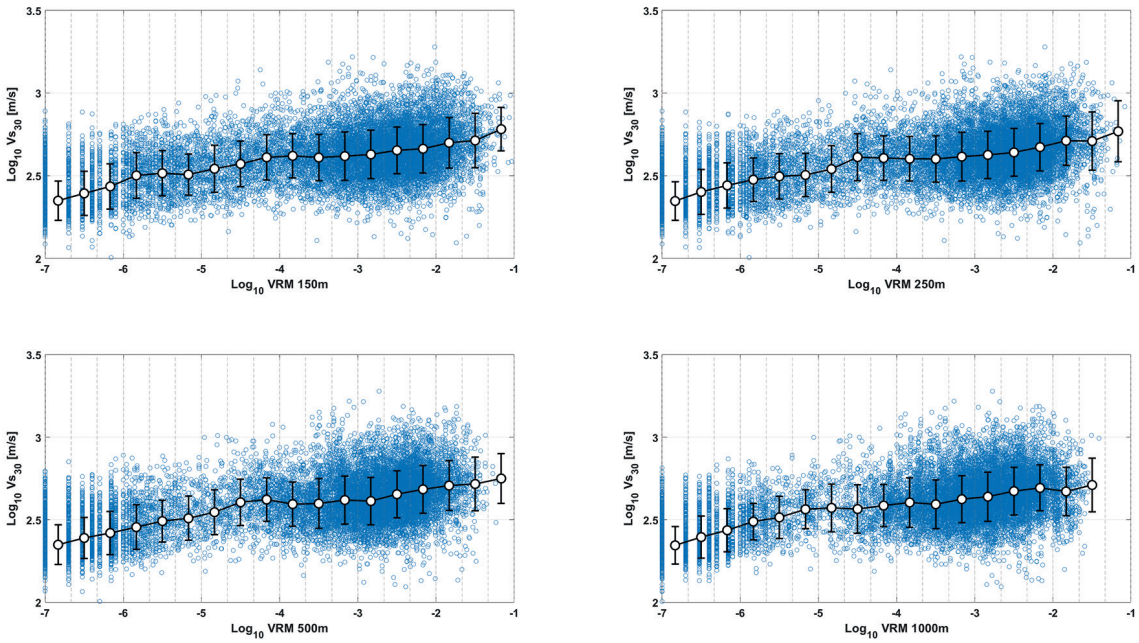

Fig. A13 - Scatter plot between $\log_{10}$*Vs*30 [m/s] and $\log_{10}$(*VRM*). The white markers and error bars indicate the mean and standard deviation within each bin (grey vertical dashed lines).

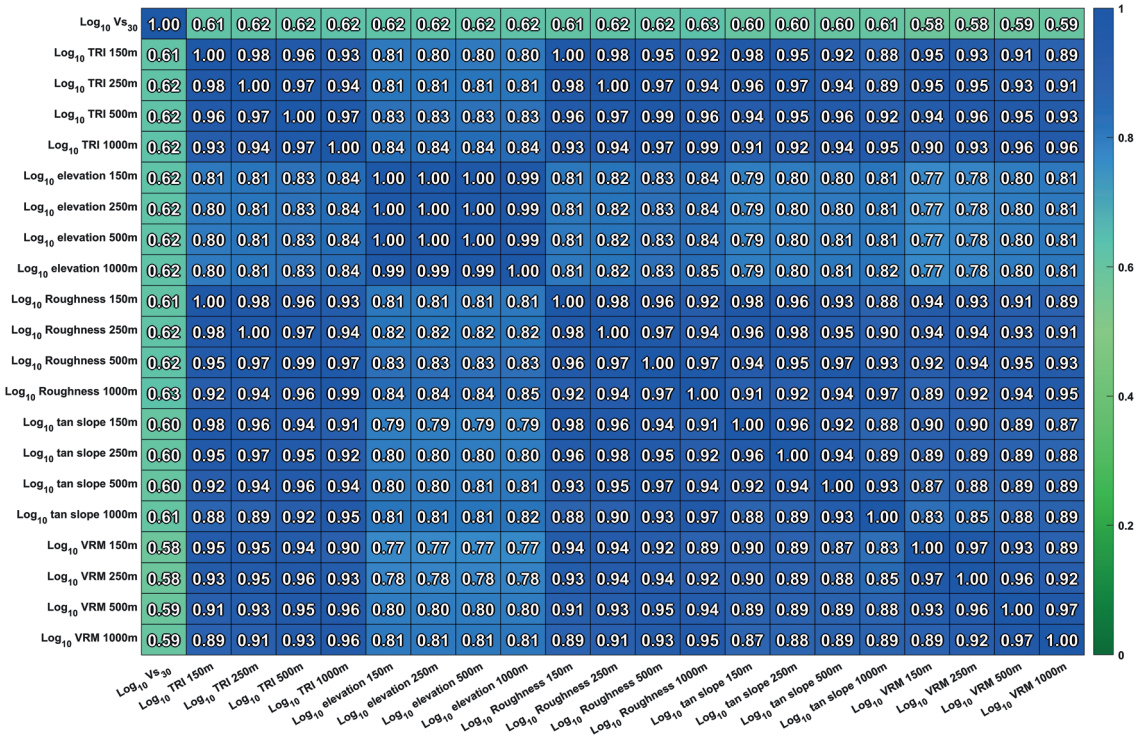

Fig. A14 - Pearson correlation matrix of the selected $\log_{10}$-transformed topographic proxies and $\log_{10}$(*Vs*30), showing both their correlations with $\log_{10}$(*Vs*30) and their mutual inter-correlations. Colour intensity represents the magnitude of *r* (0–1). The first row and the first column indicate the correlation between the $\log_{10}$(*Vs*30) and each proxy.

Table A1 - List of lithological classes and associated codes as defined in the ISPRA (2021) lithological map.

Lithology	ISPRA lithological code
Limestones	A1
Pelitic-arenaceous complexes	A10
Calcareous-arenaceous complexes	A11
Evaporites	A12
Residual rocks	A13
Cemented debris	A14
Travertines	A15
Dolomites	A2
Marly limestones	A3
Jasper	A4
Quarzarenite	A5
Diatomite	A6
Marls	A7
Conglomerates	A8
Sandstones	A9
Predominantly clayey soils	B1
Predominantly sandy soils	B2

Table A1 - continued.

Lithology	**ISPRA lithological code**
Predominantly gravelly soils	B3
Mixed-grain soils	B4
Peats	B5
Residual soils	B6
Soils with undefined grain size	B7
Chaotic marine clayey deposits	C1
Marine volcano-sedimentary complexes	C2
Felsic lavas	D1
Intermediate lavas	D2
Mafic lavas	D3
Unknown-composition lavas	D4
Pyroclastics, tuffs, ignimbrites	D5
Pyroclastics + lavas	D6
pedogenised tuffs	D7
Scoriae, lapilli, pumice, bombs	D8
Granitoid rocks	E1
Intermediate plutonic rocks	E2
Foidic plutonic rocks	E3
Phyllites and micaschists	F1
Gneiss	F2
Prasinite	F3
Ophiolites	F4
Serpentinites	F5
Contact metamorphic rocks	G1
Marbles	G2
Metamorphic dolomites	G3
Quartzites	G4
Granulites	G5
Low-grade metamorphic rocks	H1
Mineralisations of particular interest	H2
Waters and glaciers	N1
Anthropic settlements	N2
Landfills	N3

Table A2 - List of lithological classes and associated codes as defined in the lithological map of Italy by Bucci *et al.* (2021, 2022).

Lithology	**Bucci *et al.* (2021, 2022) lithological code**
Alluvial and marine deposits	Al
Unconsolidated clastic rocks	Ucr
Carbonate rocks	Cr
Siliciclastic sedimentary rocks	Ssr
Schistose metamorphic rocks	Sr
Consolidated clastic rocks	Ccr
Intrusive rocks	Ir
Non-schistose metamorphic rocks	Nsr
Pyroclastic rocks	Pr
Mixed sedimentary rocks	SM
Glacial drift	Gd
Chaotic - mélange	Cm
Lavas and basalts	Lb
Marlstone	M
Evaporite	E
Lakes and ice	Li
Beach deposits	B
Mass wasting material	Mw
Anthropogenic deposits	Ad